13

Physical and chemical principles of pulsed microplasma formation of micron-precision oxide coatings

© A.I. Mamaev, V.A. Mamaeva, Yu.N. Bespalova

Tomsk State University,
634050 Tomsk, Russia
e-mail: aim1953@yandex.ru

Received June 21, 2023
Revised September 26, 2023
Accepted September 26, 2023

The main factors influencing the parameters of pulsed microplasma oxidation and the mode of motion of the electrolyte in hydrodynamic boundary layers on the physics and chemistry of microplasma processes in aqueous solutions of electrolytes are determined. As a result of mathematical modeling of microplasma processes, an equation was obtained that relates oxidation parameters, electrolyte characteristics, spatial parameters, thickness of the porous oxide layer and discharge burning duration. The influence of viscosity and mode of motion of the electrolyte on the current-voltage characteristics, reflection spectra and surface structure of coatings is shown. It has been proven that pulsed microplasma oxidation at short voltage pulse durations makes it possible to control the characteristics of the coating and create micron-precise porous structures of a given structure.

Keywords: oxide coatings, microplasma oxidation, electrolyte, porous layer, Prandtl layer.

DOI: 10.61011/TP.2023.11.57499.154-23

Introduction

Microplasma processes in aqueous electrolyte solutions initiated by the effect of high polarizing voltages on the „electrolyte–electrode“ interface have been described earlier as a specific kind of glow [1]. Currently, microplasma processes are being studied extensively [2–5], they are being increasingly more widely used for production applications [5–8] covering such sectors as the development of functional and catalytic coatings on titanium [4–8], magnezium [9], aluminium, etc.

Formation of coating is followed by interconnected physical, chemical, electrochemical and microplasma processes, each of them having a different instantaneous velocity both throughout the process and during a voltage pulse duration. The velocity is linked to pulsed microplasma oxidation (PMPO) conditions. Changing of PMPO parameters such as polarizing voltage, voltage pulse width, oxidation duration, electrolyte composition, flow mode and rate, etc. may cause changes in the oxide coating structure, properties and functionality. Numerous factors that affect coating properties not only makes problems, but also allows to design coatings with controlled regular composition, configuration and properties. This is particularly important when making regular microstructures for microcomputer and microelectronics parts.

For treatment of large parts, different quality of coatings becomes apparent in different surface areas to be treated. Preservation of coating quality all over the surface to be machined is essential for PMPO applications.

Electrolyte flow pattern near the surface to be machined is one of the most significant factors that influence the coating quality. Pulse microplasma discharge behavior depending on the electrolyte flow modes has not been simulated before because accurate measurements are complicated or impracticable. Identification of physical and chemical principles of self-organization of a collective pulsed microplasma process in solutions will make it possible to solve such problems to a certain extent.

The goal is to identify and simulate physical and chemical patterns of formation of micron-accurate functional porous oxide coatings in the pulsed microplasma oxidation conditions considering the hydrodynamic effect.

1. Mathematical simulation of discharge in aqueous solutions

According to one of the points of view [10–14], when electrolyte is heated, its components undergo transformations from liquid to gaseous state, a local gas-vapor region occurs where breakdown and microplasma discharge take place. We assume herein that mere heating is not sufficient for discharge to occur — it primarily requires high current density and the same electric field strength exceeding the dielectric strength of the substrate material (metal). Processes (mass transfer, concentration flows and current distribution and others, whose values and spatial distribution depend on pulse width) in the Prandtl layer and porous coating thickness are addressed herein. Electrolyte in these layers is believed to be weakly mixable. The highest electric field strength and current occur in those layers whose thickness is close to submicron and micron sizes. Breakdown occurs in pores filled with electrolyte. This is exactly the layer where discharge occurs, one pole of which is attached at the metal–solution interface in a

pore and the second pole moves into the solution through the Prandtl layer as the discharge is developing (during the pulse duration). There are two main causes of charge decay. The first cause — the arc length increases resulting in lower electric field strength in the discharge, then the discharge decays. The second cause is the pulse width (when external impact stops, the arc decays). Extinction at constant current or constant voltage occurs when the arc length achieves the Prandtl layer. The arc length increase is also influenced by the electrolyte flow velocity in the Prandtl layer. These parameters are included in the equations shown herein.

Initial pulsed mictroplasma process stages as well as electrochemical-to-plasmachemical reaction transition patterns have been described for PMPO earlier [8].

At least two conditions are necessary for discharge to occur and be maintained:

1. Discharge occurs in the point where energy flux density is higher than the material's chemical bond energy resulting in formation of ions and radicals capable of current carrying.

2. Discharge is concentrated in the area of high electric field strengths.

These are the two conditions that govern the size (thickness) of the microplasma space — hydrodynamic boundary layer region where microplasma processes are concentrated.

Microplasma discharge in a solution may not be treated as dielectric breakdown. This is a breakdown in electrolyte with high inorganic salt and acid concentration. Electric current is carried by ions in the arc cord, therefore concentration distribution of ions depending on external effects shall be found for electric field strength simulation. Potential connection to the electrode is the initiating process — this ensures the start of electrode reactions. With high potentials, electrochemical reaction rate is high, but the concentration of ions involved in reactions of the electrode surface becomes equal to zero after a period of time. The process is limited by ion delivery from the electrolyte solution depth through a weakly mixable near-electrode Prandtl layer. In the near-electrode region, ion distribution with high concentration gradient is formed and depends on the voltage pulse width and shape. Low ion concentration near the electrode surface results in high electrolyte resistance (R) in the near-electrode layer, and the high ion concentration gradient results in high densities of charged particle fluxes (I) towards the surface (high current density). High-energy fluxes (Q) are concentrated in this layer ($Q = I^2Rt$). This results in microplasma discharge initiation [8]. In a porous oxide layer, reactions proceed between metal and electrolyte both inside pores and in the hydrodynamic boundary Prandtl layer [15,16]. Discharge in the anode mode causes heating of a local area on the oxidized valve metal surface to high temperature; a gas-vapor region is formed; electrode and spontaneous high temperature chemical reactions between metal and water are initiated. Thus, composite oxides of basic metal and metal oxides injected into the electrolyte are produced and may be involved in the formation of complex coatings.

Discharge simulation considering the hydrodynamic factor is based on the following provisions and assumptions:

1. Microplasma process — collective arcing of multiple discharges.

2. A single discharge has cathodic and anodic arc regions located at the metal-electrolyte interface, including the porous oxide layer. The oxide layer has high resistance and does not conduct current. The microplasma process flows on cracks and pores in the coating filled with electrolyte.

3. Changes in charge carrier concentration are within the hydrodynamic boundary layer and cover the oxide layer pores and cracks. Concentration in the electrolyte volume remains unchanged. The microplasma space thickness depends on the charge carrier (ion) distribution and electric field strength in the boundary layer between the zero ion concentration point (electrode surface) and the point where the electrolyte ion concentration is equal to the volume concentration.

4. Discharge cord is both in the oxide layer pores and in the electrolyte. When the electrolyte is flowing, a part of the cord beyond the pores in the boundary layer is displaced at the electrolyte flow rate.

5. The electric field strength is uniform throughout the arc length.

The discharge decays when the electric field strength achieves the arc extinction strength [17].

Liquids have internal frictions and, therefore, the electrolyte layers at the electrode surface boundary feature hindered convective mixing near the „electrolyte−electrode" interface that affects ion distribution when electrochemical reactions are initiated. At high polarizing voltages and high electrochemical reactions rates, the ion concentration distribution $C(x, \tau)$ in the diffusion layer is calculated as follows

$$C(x, \tau) = C_{vol}\mathrm{erf}\left(\frac{x}{2\sqrt{D_e\tau}}\right), \qquad (1)$$

where C_{vol} is the ion volume concentration, x is the distance to the electrode surface, D_e is the effective ion diffusion constant in the electrolyte, τ is the voltage pulse width [8,17–20].

Figure 1 shows that the electrolyte mixing rate (curve *2*) influences the ion concentration distribution (curve *1*). This influence increases with distance from the electrode surface and decreases with reduction of the concentration change region.

Thickness of the microplasma space where microplasma discharges are concentrated depends on change in charge carrier (ion) concentrations, voltage distribution and electric field strength. Discharge sizes depend on many factors. Similar to the approaches developed by Prandtl for hydrodynamics and by Nernst for concentration layers [15,16], define the average thickness (l_{mean}) of the microplasma space as a position of the point of intersection between the ion volume concentration and derivative ion concentration

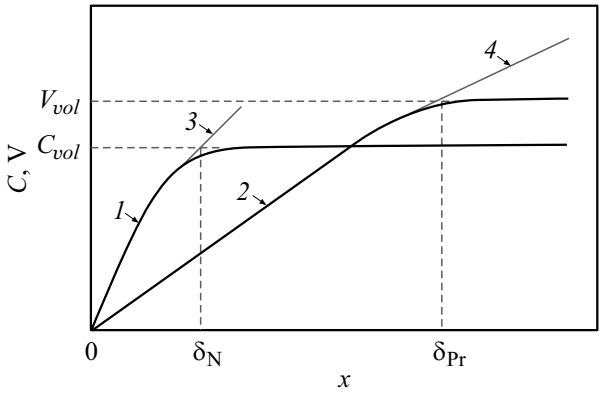

Figure 1. Dependence of the concentration distribution and liquid flow rate on the distance to the surface (x): *1* — ion concentration distribution, *2* — electrolyte flow rate distribution in the hydrodynamic boundary Prandtl layer, *3* — Nernst's microplasma space thickness (δ_N), *4* — boundary Prandtl layer thickness (δ_{Pr}).

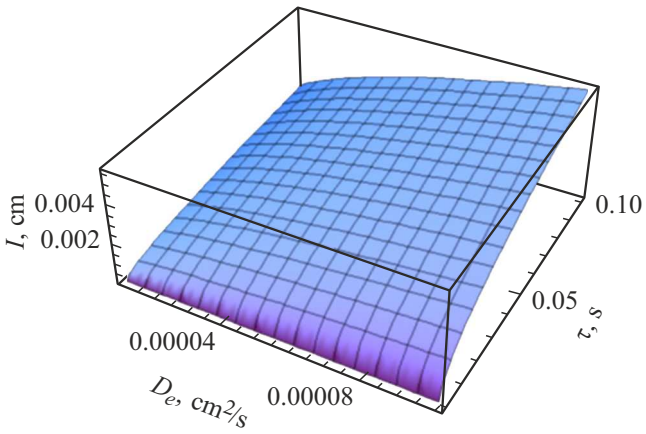

Figure 2. Dependence of the average microplasma space thickness on pulse width and effective ion diffusion constant.

on the surface:

$$l_{mean} = C_{vol} \cdot \left(\frac{dC}{d\tau}\right)^{-1} = \sqrt{\pi D_e \tau}\, \exp\left(\frac{x^2}{4D_e\tau}\right). \quad (2)$$

Average microplasma space thickness depends on pulse width and effective ion diffusion constant (Figure 2).

As shown in Figure 2, the average microplasma space thickness increases with pulse width and effective diffusion constant.

Electrolyte flow mode in the near-electrode layer is another factor affecting the microplasma space thickness. Since Nernst's microplasma space thickness is lower or equal to the hydrodynamic boundary Prandtl layer (Figure 1), the displaced anodic region of the discharge will be inside the boundary Prandtl layer or will achieve its boundary at large polarizing voltage pulse widths.

The hydrodynamic boundary Prandtl layer thickness on the fixed metal electrode plate depends on the distance from the flux run-on point (time when the electrolyte flow meets the plate) both in laminar and turbulent electrolyte flow mode (Figure 3). At the hydrodynamic layer boundary, the electrolyte flow rate is equal to the volumetric flow rate (V_{vol}). Inside this layer, the rate varies linearly from zero to V_{vol} (Figure 1).

For the rotating electrode, the near-boundary layer thickness δ_{Pr} depends only on the electrode rotating rate and, according to Prandtl [9], is calculated as follows

$$\delta_{Pr} = 3V_{vol}^{-0.5}\nu^{0.5}l_s^{0.5}, \quad (3)$$

where l_s is the distance from the flow run-on point, ν is the kinematic viscosity.

The microplasma discharge occurs in point $(l_{01}, 0)$ on the plate surface; initially, it is perpendicular to line $(l_{01} - \delta_0)$ in the coating pores and in the electrolyte layer as well (Figure 3,*a*). During discharge arcing, a ionized gas-vapor region is formed, and this increases the microplasma space thickness (Fgure 2). During experimental investigations, immediate release of gas-vapor bubbles from the surface normal to the surface at a rate up to 1 cm/s is visually observed at a distance up to 8 mm from the electrode surface.

Figure 3, *b* shows that the boundary Prandtl layer thickness (δ_0) is constant, except the initial portion.

Taking into account expansion of the gas-vapor region, the microplasma space behavior may be described as follows

$$l_{mean} = \sqrt{\pi D_e \tau} \cdot \exp\left(\frac{(x + m\tau)^2}{4D_e\tau}\right), \quad (4)$$

where*m* is the gas-vapor region length rate of change. Due to the electrolyte flow, the anodic arc region is displaced along the line between the points (l_{01}, a) and(l_1, δ_1) (Figure 3, *a*). The displacement depends on the electrolyte flow rate and microplasma space thickness. According to the Prandtl representations [9,21], the electrolyte flow rate within the hydrodynamic boundary layer varies linearly and achieves the volumetric rate at the boundary layer boundary.

The discharge arc length (l_{arc})changes according to the discharge arcing time, because the microplasma space thickness grows and the anodic arc region is displaced due to the electrolyte flow

$$l_{arc} = \sqrt{(l_{mean})^2 + (V_{vol}\tau)^2} + a. \quad (5)$$

Taking into account expression (3) and assuming that the electrolyte flow rate (Figure 1) within the boundary layer changes linearly with the distance to the surface, we get

$$l_{arc} = a + \left(\left(\frac{\tau V_{vol}(\pi D_e\tau)^{0.5}\exp\left(\frac{(x+m\tau)^2}{4\pi D_e\tau}\right)}{3V_{vol}^{-0.5}\nu^{0.5}l_s^{0.5}} - a\right)^2 + \left((\pi D_e\tau)^{0.5}\exp\left(\frac{(x+m\tau)^2}{4\pi D_e\tau}\right) - a\right)^2\right)^{0.5}. \quad (6)$$

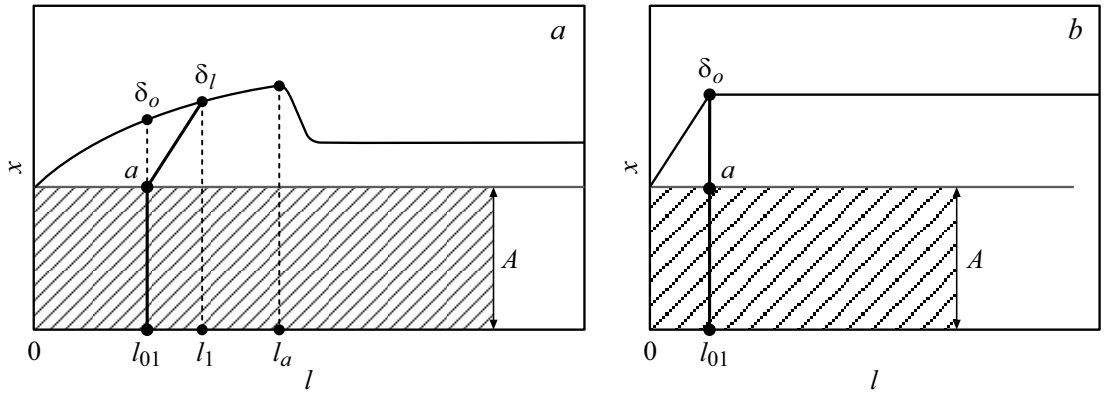

Figure 3. Dependence of the boundary Prandtl layer thickness along the plate surface: x is the distance to the electrode surface, δ_0 is the boundary Prandtl layer thickness, 0 is the electrolyte flux run-on point, $(l_{01}, 0)$ is the microplasma discharge occurrence point, a is the porous coating thickness A; a — for fixed plate in laminar and turbulent electrolyte flow modes: l_a is the laminar layer length (point of transition from laminar to turbulent mode), line $(l_{01}-l_1)$ is the displacement of the anodic arc region from point (l_{01}, δ_0) to point (l_1, δ_1) during its arcing period, line $(a-\delta_1)$ between points $(l_{01a}, l_1\delta_1)$ is the displacement line of the anodic arc region between the points during arcing period invoked by the electrolyte flux; b — for rotating electrode in laminar electrolyte flow mode.

With the electric field strength uniformly distributed over the discharge arc length, the following is true

$$E = \frac{U}{l_{arc}} =$$

$$= U \Bigg/ \left[a + \left(\left(\frac{\tau V_{vol} (\pi D_e \tau)^{0.5} \exp\left(\frac{(x+m\tau)^2}{4\pi D_e \tau} \right)}{3 V_{vol}^{-0.5} \nu^{0.5} l_s^{0.5}} - a \right)^2 \right.$$

$$\left. + \left((\pi D_e \tau)^{0.5} \exp\left(\frac{(x+m\tau)^2}{4\pi D_e \tau} \right) - a \right)^2 \right)^{0.5} \Bigg], \qquad (7)$$

where E is the electric field strength, U is the polarizing voltage.

Discharge extinction condition

$$E - E_{\text{quench}} = \frac{U}{a + \sqrt{\delta^2 + (\tau V_{vol})^2}} - E_{\text{quench}} = 0, \qquad (8)$$

where E is the electric field strength over the discharge arc length, E_{quench} is the discharge extinction strength.

Relationship (8) is used to get equation (9) that interconnects the PMPO parameters (polarizing voltage U, pulse width τ), electrolyte properties (electrolyte flow rate, volumetric electrolyte flow rate V_{vol}, kinematic fluid viscosity ν, effective diffusion constant D_e, electrolyte composition (hidden in such parameter as the electrolyte resistance from Ohm's law $U = IR$), spatial parameters (distance from the flow run-on point l_s, distance to the electrode surface x), porous oxide layer thickness a and

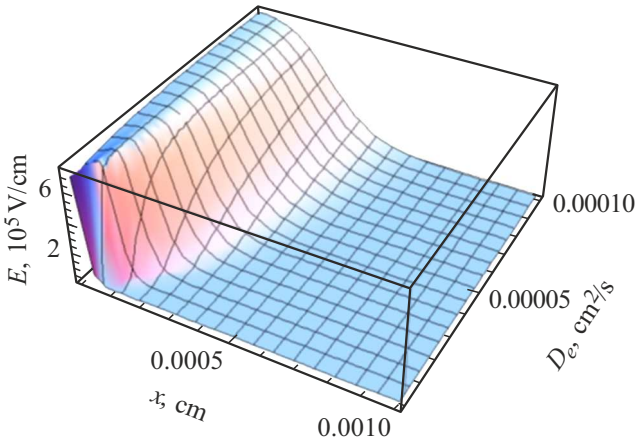

Figure 4. Dependence of the electric field strength on the distance to the electrode surface and on the effective diffusion constant at $V_{vol} = 5$ cm/s, $U = 300$ V, $l_s = 1$ cm, $a = 2\,\mu$m, $\tau = 200\,\mu$s.

discharge arcing time $t_{disch.comb}$:

$$U \Bigg/ \left[a + \left(\left(\frac{\tau_s V_{vol} (\pi D_e t_{disch.comb})^{0.5} \exp\left(\frac{(x+m\tau_s)^2}{4\pi D_e t_{disch.comb}} \right)}{3 V_{vol}^{-0.5} \nu^{0.5} l_s^{0.5}} - a \right)^2 \right.$$

$$\left. + \left((\pi D_e t_{disch.comb})^{0.5} \exp\left(\frac{(x+mt_{disch.comb})^2}{4\pi D_e t_{disch.comb}} \right) - a \right)^2 \right)^{0.5} \Bigg]$$

$$- E_{\text{quench}} = 0. \qquad (9)$$

Electric field strength distribution in the microplasma space and electric field strength behavior depending on the effective diffusion constant is shown in Figure 4.

As shown in Figure 4, with increasing effective diffusion constant, the electric field strength covers a wider near-electrode layer region.

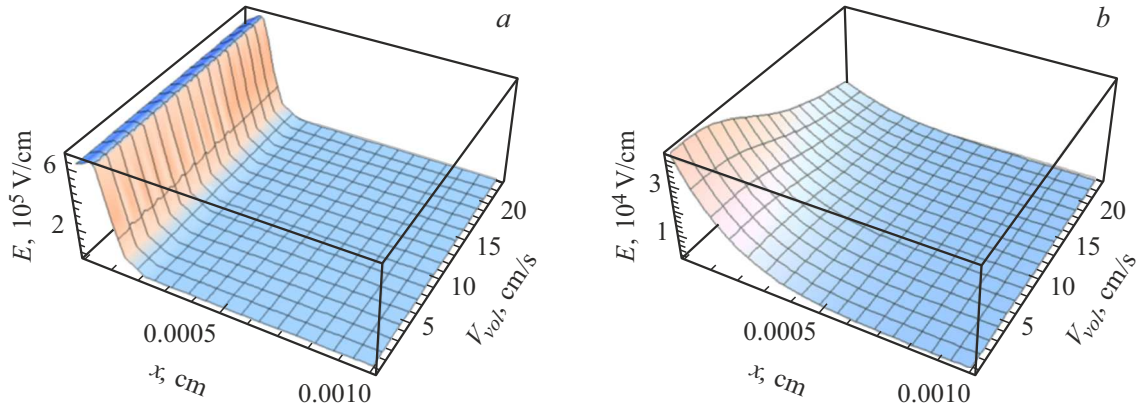

Figure 5. Dependence of the electric field strength on the distance to the electrode surface and on the volumetric flow rate of the electrolyte at $D_e = 0.00001\,\text{cm}^2/\text{s}$, $U = 300\,\text{V}$, $l_s = 1\,\text{cm}$, $a = 2\,\mu\text{m}$ for: a — $\tau = 200\,\mu\text{s}$, b — $\tau = 10000\,\mu\text{s}$.

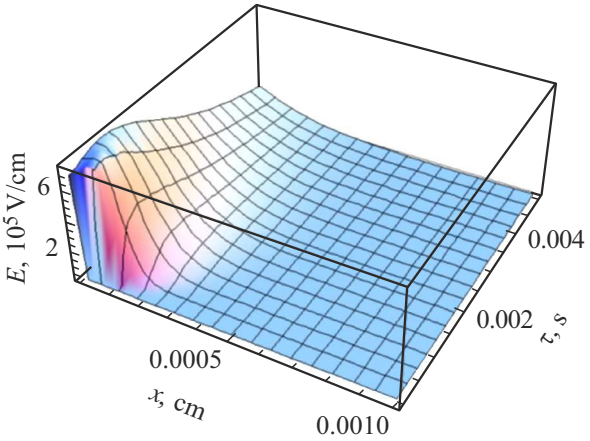

Figure 6. Dependence of the electric field strength on the distance to the electrode surface and on the pulse width at $D_e = 0.00001\,\text{cm}^2/\text{s}$, $U = 300\,\text{V}$, $l_s = 1\,\text{cm}$, $a = 2\,\mu\text{m}$.

Dependence of the electric field strength on the volumetric electrolyte flow rate is shown in Figure 5.

At low pulse widths (Figure 5, *a*), high electric field strength is concentrated at the phase interface and weakly depends on the volumetric electrolyte flow rate. At high pulse width (Figure 5, *b*), increasing volumetric electrolyte flow rate results in sharp decrease of the electric field strength.

Figure 6 shows the dependence of the electric field strength on the distance to the electrode surface and on the pulse width.

Relation (7) and Figures 4–6 show that narrow current pulses result in high electric field strength at the phase interface.

The electric field strength decreases with increasing rate of change of the gas-vapor region length (Figure 7) and depends on the thickness of coating formed during PMPO (Figure 8).

With coating thickness growth, the electric field strength decreases (Figure 8). This proves the previous well-known experimental data showing that the polarizing voltage must be increased to increase the coating thickness. Maintenance of constant voltage results in pore refilling and wide variety of pore sizes.

Anodic oxide film is about some micrometers in thickness. For simulation purposes (Figure 8), however, it would be interesting to address an oxide film with even less thickness, when the electric field strength and current density are as high as possible causing microplasma discharge to occur. When the pulse exists, the discharge first develops, then its arc length increases and finally the discharge decays. It is at the pulse start when pores are formed and cause dielectric strength vulnerability of the coating. This process is simulated and shown in Figure 8, when porosity is formed at the initial coating growth stage: coatings up to $35\,\mu\text{m}$ in thickness with controlled porosity and pore sizes are formed in such conditions.

Changing the pulse width allows control of the microplasma space size, electric field strength distribution in

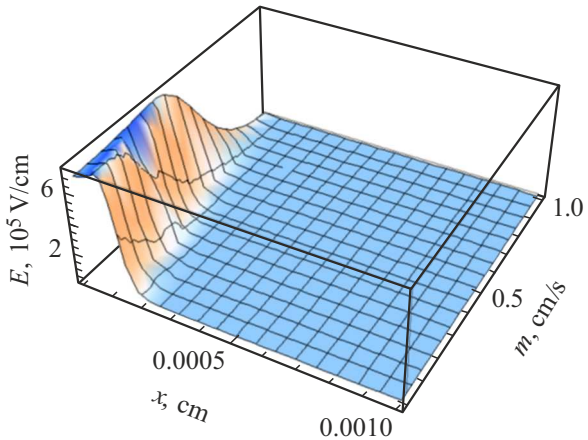

Figure 7. Dependence of the electric field strength on the distance to the electrode surface and on the rate of change of the gas-vapor region length at $D_e = 0.00001\,\text{cm}^2/\text{s}$, $U = 300\,\text{V}$, $l_s = 1\,\text{cm}$, $a = 2\,\mu\text{m}$.

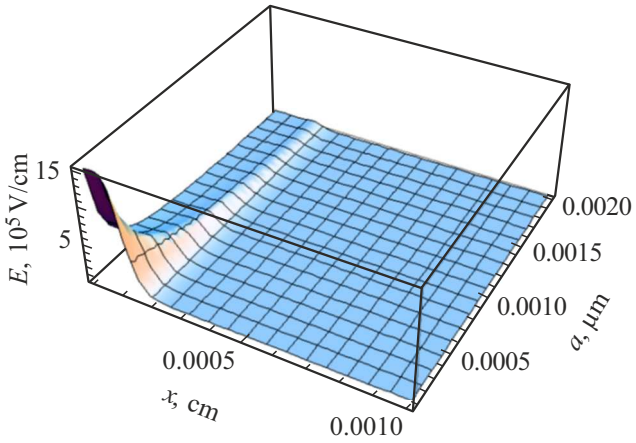

Figure 8. Dependence of the electric field strength on the distance to the electrode surface and on the coating thickness at $D_e = 0.00001\,\text{cm}^2/\text{s}$, $U = 300\,\text{V}$, $\tau = 200\,\mu\text{s}$, $l_s = 1\,\text{cm}$, $m = 0.1\,\text{cm/s}$.

the boundary layer, and coating structure. If the pulse width is such that a microplasma space is formed that is much thinner than the boundary Prandtl layer, then the oxide coating structure depends on the pulse width and polarizing voltage.

In the limiting case, when the voltage pulse width is high or voltage is constant and the anodic arc region achieves the Prandtl layer boundary and does not move any more (ion concentration at the Prandtl layer boundary is equal to the volume concentration due to the convective fluxes in the electrolyte), the coating structure depends both on the oxidation modes and the electrolyte flow rate. Discharge arcing time is calculated as follows

$$t_{disch.comb} = \frac{1}{V_{vol}}\sqrt{\left(\frac{U}{E_{disch}} - a\right)^2 - \delta_{\text{Pr}}^2}, \qquad (10)$$

where E_{disch} is the electric field strength.

Electric field strength and consequently the probability of discharge are higher when pulse widths are low. Increasing number and sizes of microplasma discharges are recorded visually with decreasing voltage pulse width, particularly when the oxide layer thickness is low.

2. Experimental

2.1. Equipment and procedure for investigating current-voltage curves

A data measurement system (DMS) designed to study high energy processes in electrolyte solutions when high-density pulse currents are carried [15,16] was used to investigate the effect of electrolyte flow modes and to record current-voltage curves (CVC). The importance of CVC recording is in that they to a certain extent correlate the rate of various process stages (current) with the process energy ($\Delta G = -zFU$) and allow approaching the instrumental study of various limiting phases on the microplasma process using the CVC analysis. The PMPO coating formation process is explained by plasma or electrochemical patterns. High temperature chemical reactions contribute to CVC and require more detailed examination.

DMS consists of a microplasma section, „SIBSPARK“ trapezoidal voltage pulse source with voltage (from 10 to 600 V) and voltage pulse width (from 10 to 300 μs) adjustment function, time-synchronized high-speed devices for digital current and voltage measurements, and measurement processing software. The microplasma section is a rotating electrode with electrode rotation control function and electrolyte pumping system for electrolyte temperature stabilization. High-speed instruments enable time-synchronized recording and digitizing of current and voltage pulses at a rate of 10^9 samples per second to record CVC at potential rates of change up to 10^8 V/c at current pulse edges. These direct measurements were used to record descending voltage pulse CVC [17,18] depending on the PMPO modes. The purpose of processing of 50 successive current and voltage pulse measurements is to calculate the average in order to reduce the noise effect.

AMg3 alloy cylinders 20 mm in diameter and 20 mm in height with threaded central hole for current collector attachment were used as the specimens. Side surface of the cylinder was insulated with a heat shrink tape. The end working surface was ground to surface finish class 7. Each specimen was used only once. Measurement and processing procedures, rotating electrode and equipment details have been provided before in [17,19].

2.2. Coating composition, morphology and spectra examination equipment and procedures

Chemical analysis of the test specimens was carried out by the energy-dispersive X-ray microanalysis methods using FEI Quanta 200 3D scanning electron-ionic microscope with AMETEK EDAX energy-dispersive microanalyzer. Chemical analysis was carried out in $0.01\,\text{mm}^2$ areas scanning mode and in $\sim 0.1\,\mu\text{m}^2$ spot mode. Measurement accuracy is maximum 5% for elements $Z > 10$.

Coating morphology was studied in secondary recording mode using FEI Quanta 200 3D scanning electron-ionic microscope at accelerating voltages of 5–10 kV.

Spectra were recorded using inVia (Renishaw, UK) Raman-scattering spectrometer with DM 2500M (Leica, Germany) microscope, 50× lens. Signal was excited by 785 nm continuous semiconductor laser. Laser power for the measurements was about 0.5 mW, spectrum recording was performed in the stokes region within $100-3500\,\text{cm}^{-1}$ (793–1080 nm) in reflection mode. Laser power was chosen such that to avoid any laser-induced changes in the test specimens. The measurements were carried out on three specimens of each type in five points each. Spectral shifts were max. 0.2 nm ($\sim 4\,\text{cm}^{-1}$ for this spectral region).

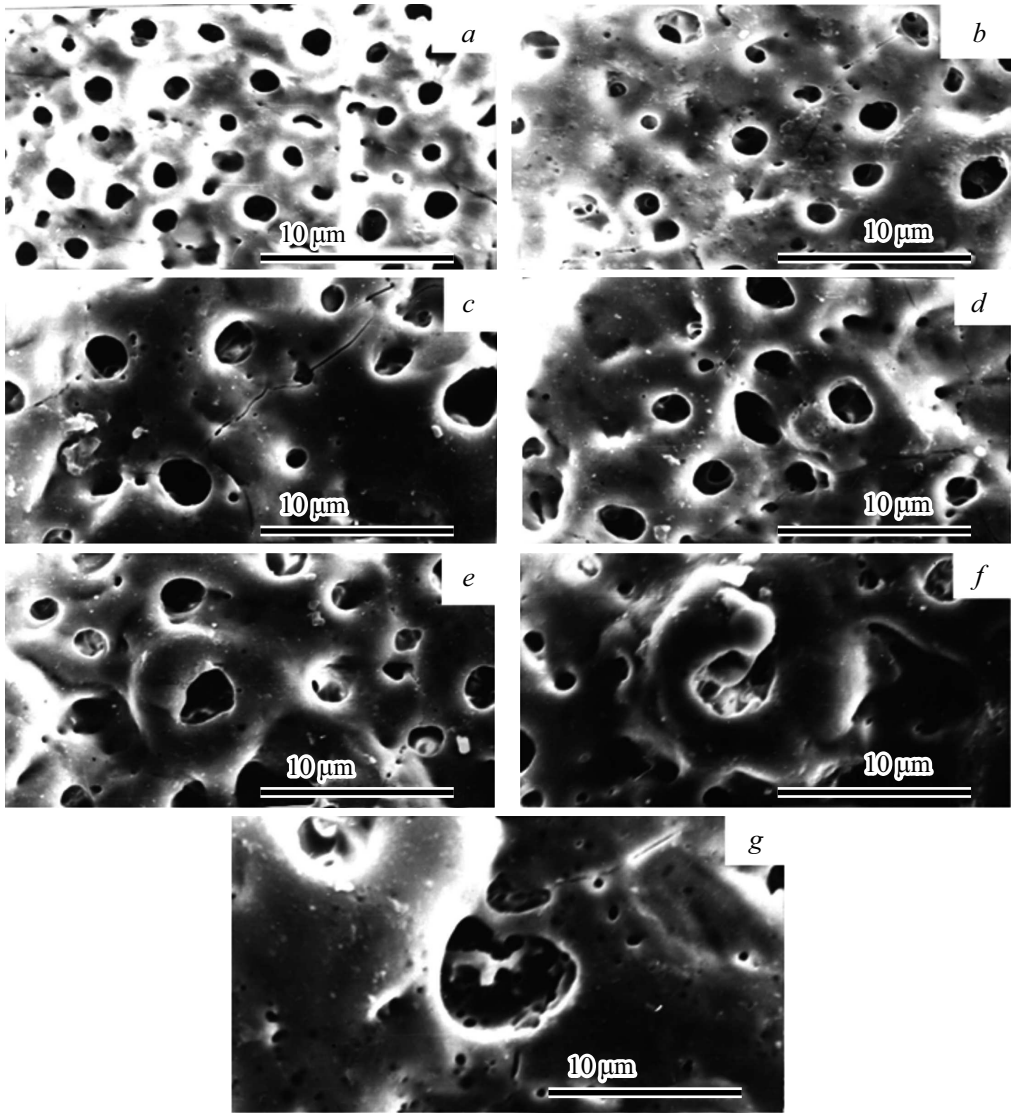

Figure 9. Pulse width effect on coating morphology (magnification×2500): *a* — 50, *b* — 100, *c* — 150, *d* — 200, *e* — 250, *f* — 300, *g* — 400 μs.

Dependence of the average pore diameter on the pulse width

Pulse width, μs	50	70	100	150	200	250	300
Average pore diameter, μm	1.94 ± 0.14	2.10 ± 0.15	3.50 ± 0.25	4.20 ± 0.29	4.70 ± 0.33	4.80 ± 0.34	4.85 ± 0.34

Quantitative spectra assessment was carried out using the analysis of the spectra recorded on the specimens with different types of treatment. Currently, the authors are working extensively on the investigation of spectrum shifts, and this will be a next separate study (publication).

2.3. Investigation of the PMPO conditions effect on the coating performance without hydrodynamic factor control

Figure 9 shows the coatings applied on AMr3 alloy without electrolyte mode and flow rate control at different pulse widths. Electrolyte composition: H_3BO_3 — 35 g/l, NaOH — 15 g/l, NaF — 10 g/l, H_3PO_4 — 11 g/l, balance — H_2O; electrolyte temperature — 25–28°C. Chemical materials grade — Ultra High Pure. $U = 350$ V, PMPO time — 600 s. At a pulse width of 50 μs , coating with uniform pore distribution on the surface are produced; pore diameters is about 2 μm. At a pulse width of 100 μs, the number of pores decreases (compared with PMPO at 50 μs), and the pore diameter increases up to 3 μm (Figure 9).

At pulse widths of 100, 150, 200 and 250 μs, pores with diameters from 3 to 5 μm are formed (see the Table).

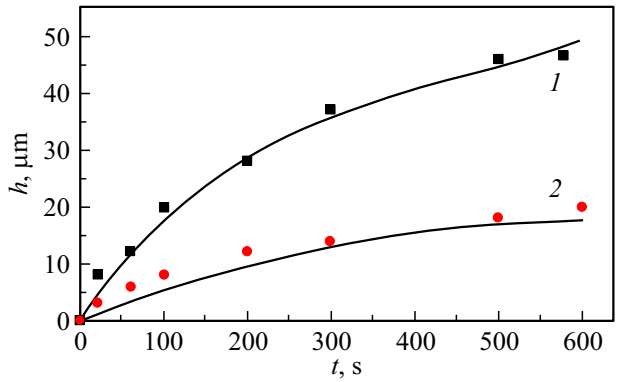

Figure 10. Dependence of the coating thickness on PMPO time for: *1* — trapezoidal pulse waveform, *2* — sinusoidal pulse half-wavelength.

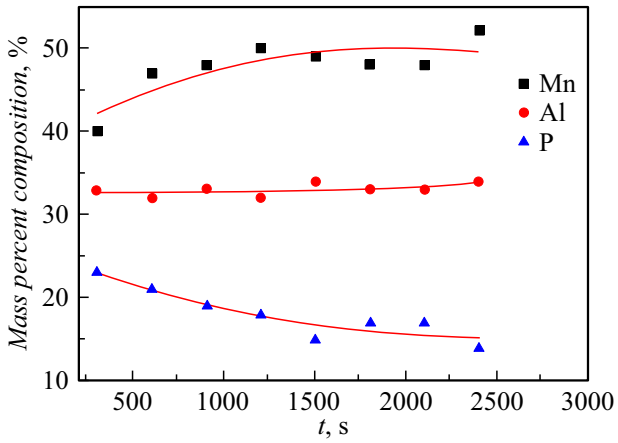

Figure 11. Elemental composition change of coatings depending on the PMPO time at $U = 350$ V, $\tau = 200\,\mu$s.

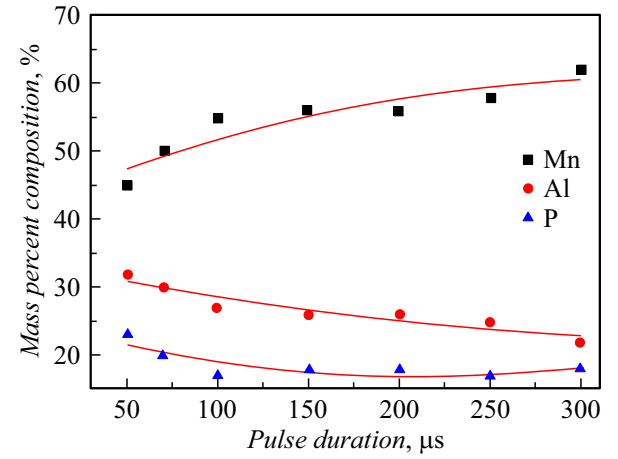

Figure 12. Elemental composition change of coatings depending on the pulse width at $U = 350$ V, PMPO time is 600 s.

Further increase in the pulse width ($300\,\mu$s and higher) and PMPO time (more than 600 s) results in pore refilling, wide scatter of pore diameters, multiple fine pores occur in breakdown areas and within large pores.

Coating growth rate decreases with increasing PMPO time for any polarizing voltage waveform (Figure 10). Electrolyte composition: H_3BO_3 — 35 g/l, NaOH — 15 g/l, NaF — 10 g/l, H_3PO_4 — 11 g/l, H_2O. $U = 350$ V, $\tau = 200\,\mu$s.

As shown in Figure 8, the coating thickness increases and electric field strength decreases (Figure 6) with increasing process time. This is typical both for trapezoidal waveform and sinusoidal half-wavelength of the polarizing voltage (Figure 10).

With increasing coating thickness, the electric field strength in the electrolyte layer decreases (Figure 8) and the microplasma space thickness decreases accordingly, therefore the elemental composition of coatings changes at high voltages.

Figures 11–14 show dependences of the elemental composition of coating on the PMPO time, pulse width, polarizing voltage and additive concentration ($KMnO_4$), respectively. For Figures 11–13, the electrolyte composition is as follows: H_3BO_3 — 35 g/l, NaOH — 15 g/l, NaF —

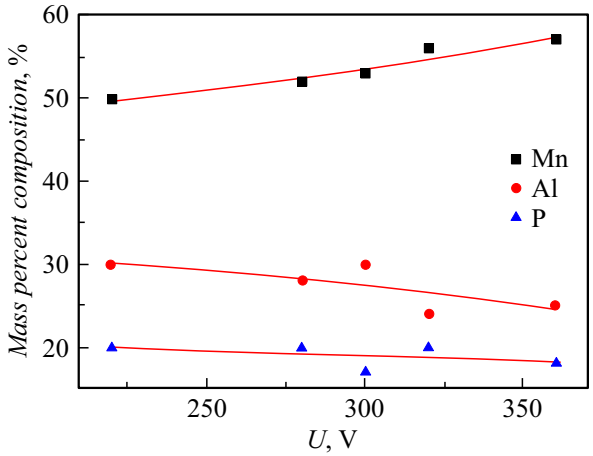

Figure 13. Elemental composition change of coatings depending on the polarizing voltage at $\tau = 200\,\mu$s, PMPO time is 600 s.

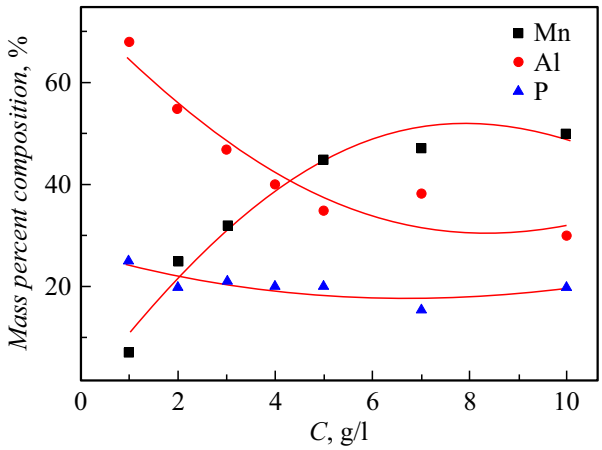

Figure 14. Elemental composition change of coatings depending on the additive concentration (C_{KMnO4}) at$U = 350$ V, $\tau = 200\,\mu$s, PMPO time — 600 s.

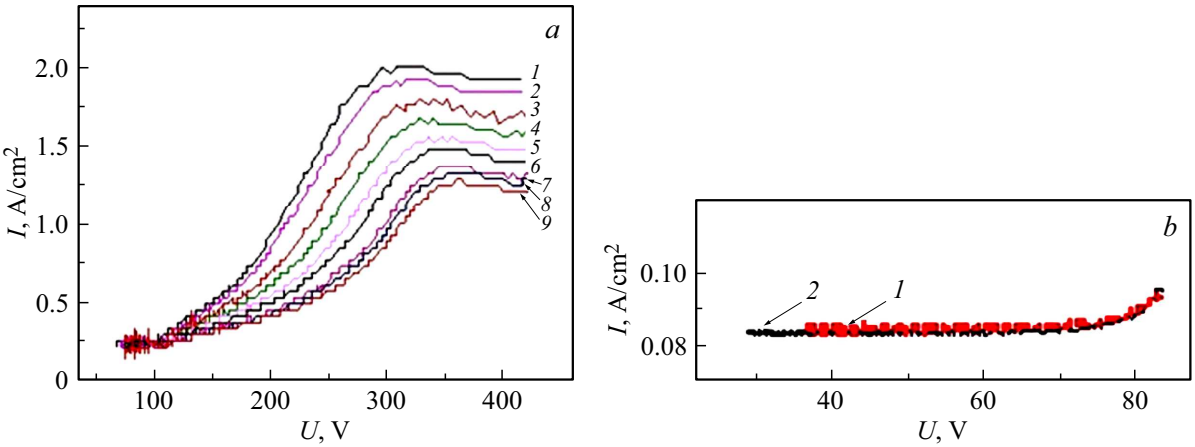

Figure 15. Dependence of CVC on the electrode rotation rate, [rpm]: *a* — in the PMPO mode: *1* — 0, *2* — 350, *3* — 610, *4* — 850, *5* — 1020, *6* — 1200, *7* — 1500, *8* — 1700, *9* — 2100; *b* — in the pulsed potentiostatic anodic coating mode: *1* — 0, *2* — 1020 [17].

10 g/l, H_3PO_4 — 11 g/l, $KMnO_4$ — 10 g/l, H_2O. For Figure 14, $KMnO_4$ concentration was varied in this electrolyte.

According to the obtained dependences (Figures 11–14), coating compositions may be controlled by changing the PMPO conditions (oxidation time, pulse width, voltage and electrolyte composition).

2.4. Electrode rotation rate effect on CVC

Different structure and thickness of the hydrodynamic boundary layer in various points of the oxidized metal surface produce different conditions for microplasma discharge occurrence. A 20 mm AMg3 rotating disc electrode [15–17], in which incoming electrolyte fluxes flow to the center of the rotating electrode and then along the rotating surface, was used to correct the effect of the boundary layer nonuniformity and to study the flow modes. Center of the disc is the flow run-on point. Change in the electrolyte flow rate depending on the disc diameter results in the fact that the boundary layer thickness depends only on the angular rotation rate of the electrode and electrolyte viscosity. In laminar electrolyte flow mode (critical Reynolds number < 2300), the boundary layer thickness is calculated as follows

$$\delta = 1.75\omega^{-\frac{1}{2}}D^{-\frac{1}{2}}\nu^{\frac{1}{6}}, \qquad (15)$$

where δ is the boundary layer thickness, ω is the angular rotation rate of the electrode, D is the molecular diffusion coefficient, ν is the kinematic viscosity.

Change in the electrode rotation rate and/or electrolyte viscosity allows the boundary layer thickness to be controlled in the laminar mode. In the laminar mode, the boundary layer thickness remains constant all over the electrode surface. The laminar mode is changed to the turbulent mode when the critical Reynolds number (2300) is achieved and is equal to 219 rpm for the 1 cm electrode; the linear flow rate limit for aqueous electrolyte is 23 cm/s.

For the turbulent flow, it is difficult to ensure constant boundary layer thickness using the rotating electrode.

Using DMS, CVC of the descending trapezoidal polarizing voltage pulse portion were recorded in the PMPO mode (Figure 15, *a*) and in the pulsed potentiostatic anodic coating mode without microplasma processes (Figure 15, *b*) for various electrode rotation rates. Electrode is the 20 mm AMg3 disc. $U = 409$ V, $\tau = 100-200\,\mu$s, treatment time is 600 s. Electrolyte composition: H_3BO_3 — 35 g/l, NaOH — 15 g/l, NaF — 10 g/l, H_3PO_4 — 11 g/l, balance — H_2O; electrolyte temperature — 25–28°C.

Current density in pulsed potentiostatic anodic coating mode without microplasma processes is much lower than the current density in the PMPO mode even at the same voltages (Figure 15). This suggests a governing influence of microplasma processes on the growth of a new oxide phase and, what is most important, a change in the nature of coating formation. And the provision that microplasma processes suppress electrochemical processes is supported. In the anodic coating mode, there is no mixing effect on the CVC parameters (Figure 15, *b*). In the PMPO mode, the CVC parameters depend on the mixing rate (electrode rotation rate (Figure 15, *a*)); the lower the polarizing voltage the lower the mixing effect. CVC variations at low pulse width are not much different from CVC at the electrode rotation rate up to 350 rpm, that corresponds to the laminar flow mode. At rotation rates higher than 350 rpm, the flow becomes turbulent, the boundary layer thickness becomes lower, the electrolyte flow rate increases and the CVC changes becomes more apparent.

2.5. Reflection spectra of coatings applied in various coating application modes

Figure 16 shows the Raman reflection spectra (at $\lambda_{ex} = 785$ nm) of coatings applied in various treatment modes of the rotating electrode (AMg3) in the following electrolytes: H_3BO_3 — 35 g/l, NaOH — 15 g/l, NaF — 10 g/l, H_3PO_4 — 11 g/l, H_2O. Treatment time is 600 s.

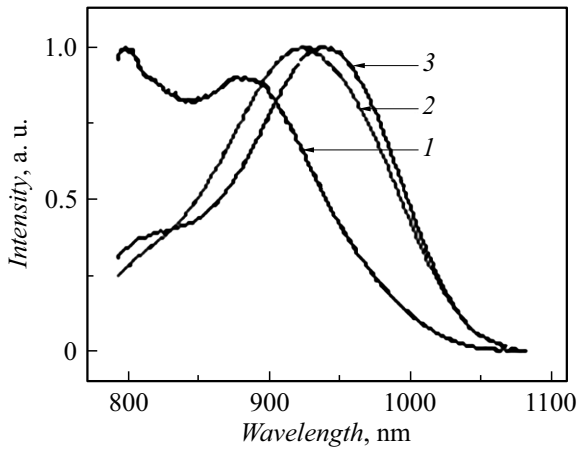

Figure 16. Reflection spectra of coatings applied in the following modes: *1* — anodic coating at $U = 100$ V, $\tau = 100\,\mu$s; *2* — PMPO at $U = 400$ V, $\tau = 100\,\mu$s; *3* — PMPO at $U = 400$ V, $\tau = 200\,\mu$s [17].

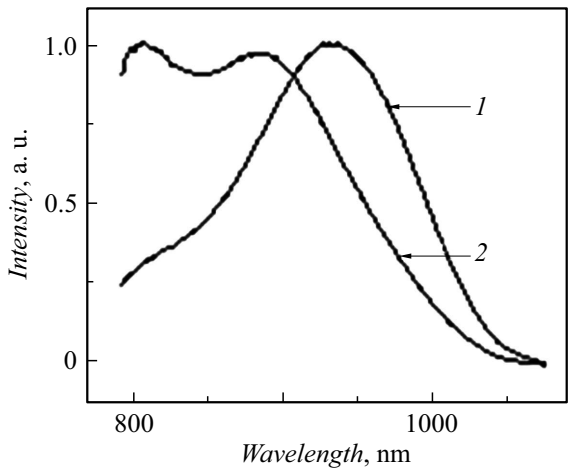

Figure 17. reflection spectra of coatings applied in the PMPO mode in the electrolyte without glycerol (*1*) and with glycerol (*2*).

Figure 16 shows that the spectrum peak shift towards larger wavelengths is observed with increasing pulse width and polarizing voltage.

2.6. Reflection spectra of coatings applied in electrolytes with different viscosity

Electrolytes with the same salt concentration, but different viscosity have been studied, for which glycerol has been injected in the base electrolyte. Figure 17 shows the Raman reflection spectra (at $\lambda_{ex} = 785$ nm) of coatings applied in two electrolytes. First: H_3BO_3 — 26 g/l, NaOH — 11 g/l, NaF — 7.5 g/l, H_3PO_4 — 8 g/l, H_2O. Second: H_3BO_3 — 26 g/l, NaOH — 11 g/l, NaF — 7.5 g/l, H_3PO_4 — 8 g/l, glycerol — 25 g/l, H_2O. Glycerol injection has changed the electrolyte viscosity from 1 to 1.13 mPa·s. For both electrolytes: $U = 400$ V, $\tau = 100\,\mu$s, PMPO time is 600 s.

The glycerol additive has changed the coating reflection spectrum (Figure 17), bringing it closer to the reflection spectrum of the oxide coating applied by the pulsed anode coating method (Figure 16), that is indicative of a change in the type of chemical bonds in the coating.

The glycerol additive increases the electrolyte viscosity and hydrodynamic boundary layer thickness. Moreover, the characteristic length in the dimensionless Reynolds criterion changes, which allows high quality coatings to be applied on large parts.

2.7. Investigation of the hydrodynamic factor on coating quality

The coating quality directly depends on the boundary layer structure that may be controlled by the hydrodynamic factor variation, i.e. the electrolyte flow mode that depends on the electrode rotation rate. The coating quality herein means repeatability when multiple coatings applied to the same alloy by different operators in different time, but in the same treatment conditions, have the same specifications. The method described herein allows to produce coatings that are quasiuniformly applied to the metal surface and have the same structure. It is shown that the hydrodynamic effect must be avoided to achieve such kind of coatings; in this case, the coating composition and porosity can be controlled.

In addition, performance of semiautomatic units created by the authors [8] achieves 20 000 m^2 per year. The coating quality (up to 35 μm) is accurately controlled by the coating application time, and the application modes allow accurate porosity control, therefore the coatings may be referred to as micron precision coatings.

Figure 18 shows the coatings applied at various electrode rotation rates in the following electrolytes: H_3BO_3 — 26 g/l, NaOH — 11 g/l, NaF — 7.5 g/l, H_3PO_4 — 8 g/l, H_2O. $U = 400$ V, $\tau = 200\,\mu$s, PMPO time is 600 s. Electrode rotation results in the formation of boundary layers on the electrode surface with laminar and turbulent electrolyte flow modes.

The boundary layer thickness decreases with increasing rotation rate. When the Reynolds number equal to 2300 is achieved, transition from the laminar to turbulent electrolyte flow mode is observed. As sown in Figure 18, when the electrode is rotating, coatings on its surface are destroyed. The critical electrode length corresponds to the distance of 1 cm from the center of rotation at 500 rpm. With increasing rotation rate, the radius of the unaffected surface decreases due to the change in the hydrodynamic boundary layer structure, i.e. transition from the laminar to intermediate and then to turbulent low mode. The change in the electrolyte flow rate results in the change of microplasma discharge arcing behavior and time, that affects the Raman reflection spectra of the coating (Figures 16, 17).

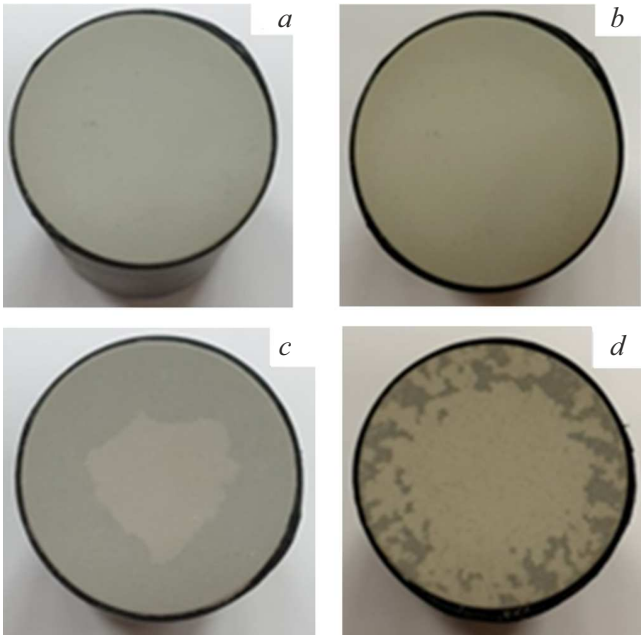

Figure 18. Types of coatings applied using a rotating electrode at different rotation rates, [rpm]: *a* — 500, *b* — 700, *c* — 1000, *d* — 1300.

2.8. Investigation of the surfaces of coatings applied at various electrode rotation rates

The use of the rotating electrode at the electrolyte flow rates within the hydrodynamic boundary layer that correspond to the laminar flow allows the layer thickness to be stabilized. The microplasma discharge properties are affected by the displacement rate of the anodic discharge arc region that depends on the electrolyte flow rate near the rotating electrode. Figure 19 show the coating surface areas formed on the rotating electrode surface at 136 rpm in the laminar electrolyte flow mode. Electrolyte: H_3BO_3 — 35 g/l, NaOH — 15 g/l, NaF — 10 g/l, H_3PO_4 — 11 g/l, H_2O. $U = 400$ V, $\tau = 150\,\mu$s, PMPO time is 600 s. The flow mode has been determined using the Reynolds number equal to 2300 and the electrode rotation rate. perturbations produced by the microplasma discharges are not addressed due to the large amount of electrolyte.

Since at 136 rpm, the electrolyte flow mode is laminar and the boundary layer thickness is constant, the coating surface differences (Figure 19) are attributed to the electrolyte flow rate only.

The Table shows average pore diameters depending on the pulse width, and Figure 19 suggests that pore specifications are the same in different points of the specimen: the average pore diameter is $4.2\,\mu$m, average pore density is $1.9 \cdot 10^6$ pores per cm^2, coating porosity is 27%. it has been shown earlier [21] that the concentration changes are deep inside the laminar boundary layer when the pulse width is $200\,\mu$s, therefore they do not affect the coating behavior and porosity. This allows to design oxide layers with pre-defined thickness, porosity and structure. In this case, porosity in the laminar mode depends on only on the polarizing voltage and pulse width. Exclusion flow run-on point. Figure 20 shows the surface areas of coatings applied in the same microplasma oxidation conditions as shown in Figure 15, but at the electrode rotation rate of 1380 rpm.

As shown in Figures 19, 20, the coating surface appearance depends on the distance from the center of the rotating electrode. In the center of the rotating electrode, the boundary layer thickness is low ($l_s = 0$ in expression (3)) [8,15,16] (Figure 19, *a*), which does not provide conditions for high density energy concentration [8].

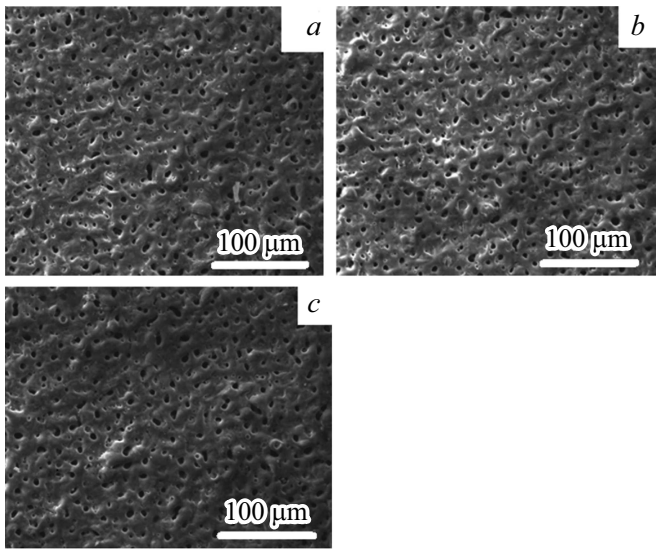

Figure 19. Surface of the coating applied using a rotating electrode (136 rpm) at distances from the center, [mm]: *a* — 1, *b* — 4, *c* — 7.

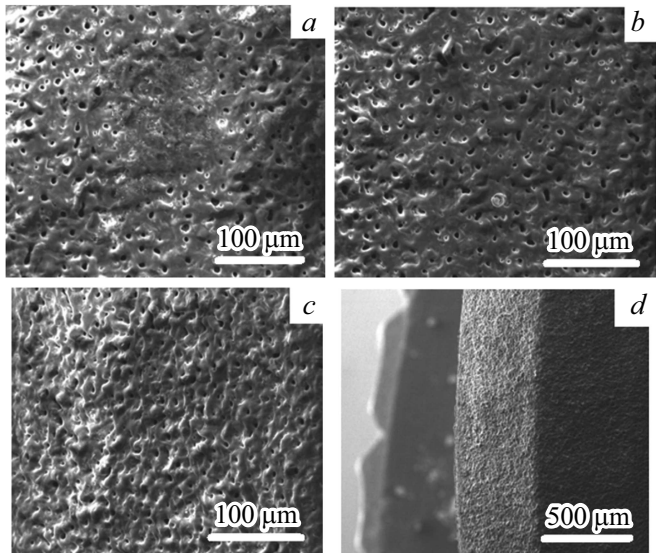

Figure 20. Surface of the coatings applied using a rotating electrode (1380 rpm) at distances from the center, [mm]: *a* — 0, *b* — 4, *c* — 7, *d* — 9.

there are no microplasma discharges and no pores accordingly in the center of the rotating electrode. At a distance from the electrode center, the boundary layer thickness remains constant resulting in constant pore density and diameter.

With increasing rotation rate, the electrolyte flow rate increases, the electrolyte flow mode changes from the laminar to turbulent mode and the boundary layer thickness decreases sharply. In this case, the number of pores increases, and the pore sizes decrease with increasing distance from the center of the rotating electrode due to the increasing electrolyte flow rate and decreasing boundary Prandtl layer thickness. Figure 20, *d* shows the boundary formed due to the changing electrolyte flow mode — in transition from the laminar to turbulent mode. In the turbulent electrolyte flow mode, the boundary layer is thinner that results in the increasing discharge density and number of pores.

Conclusion

1. Physical and chemical patterns of formation of micron-accurate functional porous oxide coatings in the pulsed microplasma oxidation conditions considering the hydrodynamic effect were identified and simulated. An equation was derived that interlinked the oxidation parameters (polarizing voltage, pulse width), electrolyte specifications (flow mode and volumetric flow rate, kinematic viscosity, effective diffusion constant of the electrolyte), spatial parameters (distance from the flow run-on point, distance to the electrode surface), porous oxide layer thickness and discharge arcing time.

2. For fixed electrode oxidation, increased pulse width and treatment time result in the increasing number of fine pores in breakdown regions and within large pores, and then in pore refilling.

3. The elemental composition of the coating is governed by the oxidation time, pulse width, polarizing voltage and electrolyte composition. During long-term oxidation, element concentrations in the coating achieve constant values.

4. The electrode rotation rate affects CVC.

5. The coating reflection spectra are affected by the oxidation mode and electrolyte viscosity. Since both electrochemical and plasma processes affect the coating formation, increasing electrolyte viscosity probably increases the aluminium oxide concentration in the coating due to the electrochemical processes.

6. There are no microplasma discharges and, therefore, no pores in the center of the rotating electrode. With increasing distance from the center and increasing electrode rotation rate, the number of pores increases and pore sizes decrease. Pore density and diameter are constant at long distance from the center.

7. The findings allow to form reproducible oxide coatings with predictable composition, quasiuniform distribution of micron-size pores and design oxide layers with a pre-defined micron-precision structure.

Conflict of interest

The authors declare that they have no conflict of interest.

References

[1] N.P. Sluginov. Zhurn. russ. phiz-khim. ob-va, **12** (1), 193 (1880).
[2] J.B. Brennan, L. Mash. USA Patent № 2346658. Publ. 18.04. 1944.
[3] G.A. Markov, G.A. Terleeva, E.K. Shulepko. *Tr. MINKh and GP im. I.M. Gubkina* (M., Rossiya, 1985), t. 185, s. 54.
[4] P.S. Gordienko, V.S. Rudnev. *Elektrokhimicheskoye formirovanie pokrytiy na aluminii i ego splavakh pri potentsialakh iskreniaya i proboiya* (Dalnauka, Vladivostok, 1999) (in Russian)
[5] Y.L. Cheng, Z.G. Xue, Q. Wang, X.Q. Wu, E. Matykina, P. Skeldon, G.E. Thompson. Electrochimica Acta, **107**, 358 (2013). DOI: 10.1016/j.electacta.2013.06.022
[6] V.S. Rudnev, M.A. Medkov, T.P. Yarovaya, P.M. Nedozorov. Russ. J. Appl. Chem., **85** (12), 1856 (2012). DOI: 10.1134/S1070427212120117
[7] V.S. Rudnev, N.B. Kondrikov, L.M. Tyrina, D.L. Boguta, M.S. Vasilieva, I.V. Lukianchuk. Ser. Kriticheskiye tekhnologii. Membrany, **4** (28), 63 (2005) (in Russian).
[8] A.I. Mamaev, V.A. Mamaeva, V.N. Borikov, T.I. Dorofeeva. *Formirovanie nanostrukturnykh nemetallicheskikh neorganicheskikh pokrytiy putem lokalizatsii vysoenergeticheskikh potokov yf granitse razdela faz* (Izd-vo Tomsk un-ta, Tomsk, 2010) (in Russian)
[9] T.A. Konstantinova, A.I. Mamaev, V.A. Mamaeva, A.K. Tchubenko. Pat. RU 2620224. Opubl. 23.05.2017, Byul. № 15.
[10] A.V. Epelfeld, P.N. Belkin, A.M. Borisov, V.A. Vasin, B.L. Krit, V.B. Lyudin, O.V. Somov, V.A. Sorokin, I.V. Suminov, V.P. Frantskevich. *Sovremennye tekhnologii modifikatsii poverkhnosti materialov i naneseniys zashchitnykh pokrytiy*. Mikrodugovoe oksidirivanie (Renome, SPb, 2017), t. 1 (in Russian).
[11] A.G. Rakoch, A.A. Gladkova, A.V. Dub. *Plazmenno-elektroliticheskaya obrabotka aluminievykh i titanovykh splavov* (Izdat. dom MISIS, M., 2017) (in Russian)
[12] A.B. Rogov, A. Matthews, A. Yerokhin. Electrochimica Acta, **317**, 221 (2019). DOI: 10.1016/j.electacta.2019.05.161
[13] J. Martin, P. Leone, A. Nominé, D. Veys-Renaux, G. Henrion, T. Belmonte. Surf. Coatings Technol., 269, 36 (2015). DOI: 10.1016/j.surfcoat.2014.11.001
[14] C.S. Dunleavy, I.O. Golosnoy, J.A. Curran, T.W. Clyne. Surf. Coatings Technol., **203** (22), 3410 (2009). DOI: 10.1016/j.surfcoat.2009.05.004
[15] B.B. Damaskin, O.A. Petry. *Vvedenie v elektrokhimicheskuyu kinetiku* (Vysshaya shkola, Moscow, 1983) (in Russian)
[16] K. Fetter. *Electrokhimicheskaya kinetika* (Khimiya, M., 1967) (in Russian)
[17] A.I. Mamaev, V.A. Mamaeva, Yu.N. Bespalova. ZhTF, **92** (4), 495 (2023). (in Russian). (9), 1440 (2022). DOI: 10.21883/JTF.2022.09.52937.90-22

[18] A.I. Mamaev, V.A. Mamaeva, A.E. Ryabikov, Yu.N. Dolgova. Protection of Metals and Physical Chemistry of Surfaces, **58** (4), 715 (2022). DOI: 10.1134/S207020512204013X
[19] A.I. Mamaev, V.A. Mamaeva,MYu.N. Bespalova, P.F. Baranov. Instruments and Experimental Techniques, **66** (2), 271 (2023). DOI: 10.1134/S0020441223010177
[20] A.I. Mamaev, V.A. Mamaeva, A.K. Chubenko, Ya.B. Kovalskaya, T.A. Konstantinova, Yu.N. Dolgova, E.Yu. Beletskaya, N.F. Kolenchin. Russ. Phys. J., **58** (12), 1720 (2016). DOI: 10.1007/s11182-016-0707-x
[21] I.V. Malyshev. *Zr- i Se-soderzhashchie oksidnye pokrytiaia na titane: zakonomernosti formorovaniya, sostav, stroenie, morfologiya poverkhnosti* (Diss. IKH DVO RAN, Vladivostok, 2017) (in Russian)

Translated by Ego Translating